FORMATION DRY-OUT FROM CO_2 INJECTION INTO SALINE AQUIFERS. PART 1, EFFECTS OF SOLIDS PRECIPITATION AND THEIR MITIGATION

Karsten Pruess[1] and Nadja Müller[2]

[1] Earth Sciences Division, Lawrence Berkeley National Laboratory
University of California, Berkeley, CA 94720

[2] Shell International Exploration and Production B.V. - Exploratory Research
Rijswijk, The Netherlands

Abstract

Injection of CO_2 into saline aquifers may cause formation dry-out and precipitation of salt near the injection well, which may reduce formation porosity, permeability, and injectivity. This paper uses numerical simulation to explore the role of different processes and parameters in the salt precipitation process, and to examine injection strategies that could mitigate the effects. The main physical mechanisms affecting the dry-out and salt precipitation process include (1) displacement of brine away from the injection well by injected CO_2, (2) dissolution (evaporation) of brine into the flowing CO_2 stream, (3) upflow of CO_2 due to gravity effects (buoyancy), (4) backflow of brine towards the injection point due to capillary pressure gradients that oppose the pressure gradient in the CO_2-rich ("gas") phase, and (5) molecular diffusion of dissolved salt. The different mechanisms operate on a range of spatial scales. CO_2 injection at constant rate into a homogeneous reservoir with uniform initial conditions is simulated in 1-D radial geometry, to resolve multi-scale processes by taking advantage of the similarity property, i.e., the evolution of system conditions as a function of radial distance R and time t depends only on the similarity variable R^2/t. Simulations in 2-D vertical cross sections are used to examine the role of gravity effects. We find that counterflow of CO_2 and brine can greatly increase aqueous phase salinity, and can promote substantial salt precipitation even in formations with low dissolved solids. Salt precipitation can accentuate effects of gravity override. We find that injecting a slug of fresh water prior to commencement of CO_2 injection can reduce salt precipitation and permeability loss near the injection well.

1. Introduction

Injection of CO_2 into saline aquifers will displace resident brine, while giving rise to interphase mass transfer of both CO_2 and water between the aqueous and CO_2-rich phases. Experimental data for water solubility in supercritical CO_2 at pressure and temperature conditions of interest for geologic storage are not available, but a theoretical model based on chemical phase equilibrium concepts suggests water solubility is only a fraction of a percent (Spycher and Pruess, 2005). Even so, continuous injection of dry CO_2 into both depleted gas reservoirs and saline aquifers may eventually lead to complete formation dry-out in the vicinity of the injection well, which will cause dissolved solids to precipitate (Pruess and Garcia, 2002; Fuller et al., 2006; Giorgis et al., 2007; Hurter et al., 2007; André et al., 2007). Formation dry-out and associated solids precipitation is well documented for aquifer gas storage systems, where halite (NaCl) is the most common precipitate (Lorenz and Müller, 2003). Salt can also precipitate and cause formation damage around wells producing from gas reservoirs with saline brine present (Kleinitz et al., 2001). Salt precipitation reduces formation porosity, and consequently also permeability and injectivity. Several studies have shown that, due to the converging-diverging nature of natural pore channels, modest reductions in porosity can generate dramatic reductions in permeability (Vaughan et al., 1986; Verma and Pruess, 1988; Pape et al., 1999; Xu et al., 2004).

This is the first ("Part 1") of a two-part series of papers that explore the processes of salt precipitation and permeability reduction near active CO_2 injection wells. The questions addressed by this research include the following. What are the processes and parameters that control salt precipitation? How does the amount of solids precipitation depend on the main parameters of the problem, such as aquifer salinity, injection rate, and formation porosity and permeability? How severe can the associated decrease in porosity and permeability be? Are there conditions where loss of injectivity could be a problem? If so, what engineering measures can be taken to mitigate the problem?

Our approach consists of using numerical simulations for the relevant flow and transport processes, and exploring system behavior as function of problem parameters. The simulations are

performed with our general-purpose reservoir simulation code TOUGH2 (Pruess, 2004), augmented with a fluid property module "ECO2N" that provides accurate fluid properties for the system water/ CO_2/NaCl for temperatures in the range from 10 - 110 ºC, pressures up to 600 bar, and salinity to full halite saturation (Pruess and Spycher, 2007). TOUGH2/ECO2N can cope with changes in phase composition, such as (dis-) appearance of phases, by switching primary thermodynamic variables. For example, in two-phase (gas-liquid) conditions, gas saturation S_g is one of the primary variables. When the aqueous phase disappears in a grid block due to dry-out from CO2 flow, the gas saturation variable is "switched" to CO_2 mass fraction X_{CO2}.

Our treatment of solids precipitation near a CO_2 injection well focuses exclusively on precipitation of dissolved salt (NaCl) during injection-induced formation dry-out. Chemical interactions between fluids and formation minerals can also give rise to precipitation and dissolution effects (Xu et al., 2007). However, such interactions are of minor importance compared to salt precipitation due to formation dry-out and are not considered in this paper. TOUGH2/ECO2N can model multiphase flow subject to viscous, capillary and gravity forces; partitioning of H_2O and CO_2 between aqueous and CO_2-rich phases (Spycher and Pruess, 2005); dependence of thermophysical properties on pressure, temperature, and composition of fluid phases; precipitation and dissolution of halite (NaCl) subject to temperature-dependent solubility; and molecular diffusion of all species in all phases. As water solubility in the CO_2-rich phase is small, typically a fraction of percent, we neglect effects of dissolved H_2O on the density and viscosity of the CO_2-rich phase. For reference, we give the governing equations solved by TOUGH2 in Appendix A. In this paper we only consider isothermal models for CO_2 injection. Non-isothermal effects could be significant if CO_2 is injected at a temperature different from that in the injection formation. Such effects will be considered in a future study.

In modeling CO_2 injection into saline aquifers, we start from simple approximations. Specifically, we begin by considering CO_2 injection into a homogeneous aquifer with uniform initial conditions in 1-D radial flow geometry. Although such a drastic simplification of the problem may not provide realistic results for site-specific conditions, it allows to gain useful insight into the injection process by exploiting the "similarity property" of the mathematical solution. Indeed, under the conditions stated above the evolution of the flow system depends on

radial distance R and time t only through the "similarity variable" $\zeta = R^2/t$, even when taking into account all non-linearities of non-isothermal multiphase flow with fluid properties dependent upon thermodynamic conditions (O'Sullivan, 1981; Pruess and Garcia, 2002; Pruess and Spycher, 2007). The similarity property may be used to transform the partial differential equations (PDEs) governing the process into ordinary differential equations (ODEs), that can be directly integrated using the "shooting method" (Press et al., 1986; Doughty and Pruess, 1992). In this paper we do not pursue a solution of the ODEs; instead we use a numerical simulation approach to directly solve mass balance equations for the system H_2O/ CO_2/NaCl. As will be seen below, the similarity property provides useful insights and constraints for system behavior, even within a numerical simulation approach.

The focus of the present study is on the quantitative aspects of salt precipitation in the vicinity of a CO_2 injection well, as induced by formation dry-out from water dissolution into the flowing CO_2 stream. We begin by presenting and discussing results for a reference case, and invoking the similarity property to generalize results obtained by numerical simulation. We then consider a pre-flush with fresh water as a means to suppress precipitation in the vicinity of the injection well, thus avoiding permeability loss and excessive pressurization. Section 4 presents sensitivity studies that explore the role of different processes and parameters on solids precipitation. Simulations in two-dimensional radial-vertical geometry (2-D R-Z) are then used to study the interplay of gravity and capillary effects, and their impacts on precipitation. Part 2 (this volume) of this series presents an analytical model that allows to calculate the amount of solids precipitation during CO_2 injection directly from fluid properties and parameters governing the multiphase displacement process, without having to resort to numerical simulations. The analytical model provides insight into the physical mechanisms during dry-out, and it offers a simple engineering approach for estimating the potential for precipitation and injectivity loss.

2. Flow Behavior

We consider a basic problem of CO_2 injection into a saline aquifer under conditions that may be encountered at a depth on the order of 1.2 km. A CO_2 injection well fully penetrates a homogeneous, isotropic, infinite-acting aquifer of 100 m thickness (Fig. 1), at conditions of 120 bar pressure, 50 °C temperature, and a salinity of 25 % by weight NaCl (250,000 ppm). CO_2 is

injected uniformly at a constant rate of 5 kg/s for a time period of 8.64×10^8 s = 10,000 days. This problem is similar to test problem #3 of a recent international code intercomparison study (Pruess et al., 2004; Pruess and Spycher, 2007).

<Fig. 1 here>

Relative permeabilities for liquid (k_{rl}) and gas (k_{rg}) were assumed as follows.

$$k_{rl} = \sqrt{S^*}\left\{1-\left(1-[S^*]^{1/m}\right)^m\right\}^2 \tag{1a}$$

$$k_{rg} = \left(1-\hat{S}\right)^2\left(1-\hat{S}^2\right) \tag{1b}$$

where $S^* = \left(S_l - S_{lr}\right)/\left(1-S_{lr}\right)$, $\hat{S} = \left(S_l - S_{lr}\right)/\left(1-S_{lr}-S_{gr}\right)$, with S_l the liquid saturation, and S_{lr}, S_{gr} the irreducible liquid and gas saturations, respectively. Eq. (1a) for liquid was developed by van Genuchten (1980); Eq. (1b) for gas is due to Corey (1954). We use van Genuchten's (1980) formulation for capillary pressure in the form

$$P_{cap} = -P_0\left([\bar{S}]^{-1/\lambda}-1\right)^{1-\lambda} \tag{2}$$

where P_0 is the strength coefficient, $\bar{S} = \left(S_l - S_{lr}\right)/\left(S_{ls}-S_{lr}\right)$, $S_{ls} \approx 1$ denotes a liquid saturation at which P_{cap} vanishes, and λ is a parameter depending on pore geometry. Formation parameters were taken as representative of "sandy clay" from a compilation of media with different textures (Carsel and Parrish, 1988), as follows: $k_0 = 33 \times 10^{-15}$ m^2, $\phi_0 = 12$ %, $S_{lr} = 0.263$, $m = 0.187$, $S_{gr} = 0.05$.

Salt precipitation is characterized by "solid saturation" S_S, which denotes the fraction of pore space occupied by solid salt, and the corresponding permeability reduction is modeled with the "tubes-in-series" model of Verma and Pruess (1988). This model has two parameters, the fractional length Γ of pore bodies, and the fraction $\phi_r = \phi/\phi_0$ of original porosity for which permeability is reduced to zero. In the presence of solid saturation S_S, the ratio of permeability k to original permeability k_0 ($S_S = 0$) is

$$\frac{k}{k_0} = \theta^2 \frac{1-\Gamma+\Gamma/\omega^2}{1-\Gamma+\Gamma\left[\theta/(\theta+\omega-1)\right]^2} \quad (3)$$

where

$$\theta = \frac{1-S_s-\phi_r}{1-\phi_r} \quad (4)$$

depends on the fraction $1\text{-}S_S$ of original pore space that remains available to fluids, and on the parameter ϕ_r. The parameter ω is given by

$$\omega = 1+\frac{1/\Gamma}{1/\phi_r-1} \quad (5)$$

We choose parameters $\Gamma = 0.8$, $\phi_r = 0.9$, similar to what was used in a recent study of permeability changes due to precipitation of amorphous silica at a geothermal injection well in the Philippines (Xu et al., 2004). As seen in Fig. 2, this parametrization yields a very severe reduction in permeability for a modest porosity decrease, and for the particular parametrization used here can be well fit by a power law with an exponent of 2.

<Fig. 2 here>

The numerical simulations use relatively fine space discretization with a total of 800 grid blocks (Table 1), to be able to achieve good spatial resolution and limit discretization errors. In a zone surrounding the wellbore radius $R_w = 0.1$ m, up to R = 10 m where dry-out and precipitation are expected, we specify 495 grid increments of $\Delta R = 0.02$ m (see Table 1). At larger distance gridding becomes increasingly coarse. The grid is extended to a large outer distance of 10^5 m, where boundary conditions are maintained constant at initial values, to achieve an infinite-acting system.

<Table 1 here>

Simulation results for fluid and solid saturations and pressures for a case in which capillary pressures are neglected are given in Figs. 3-5 as functions of the similarity variable R^2/t. These plots can be viewed as a spatial profile at fixed time, with distance R increasing to the right, or they can be read as depicting the time dependence of conditions at a fixed radial distance, with conditions moving from the right at early time to the left at late time. It is seen that the simulated results are consistent with the similarity property. Snapshots of spatial profiles of phase saturations and pressure generally coincide closely with time dependence at a fixed distance when plotted as function of R^2/t. Some discrepancies in fluid pressures are visible near $R^2/t = 10^{-5}$ m^2/s (Fig. 5); these reflect space and time discretization effects.

The outstanding characteristic of the displacement process is the presence of sharp moving fronts. We have the gas saturation front at $\zeta_f = R^2/t \approx 10^{-3}$ m^2/s, and the dry-out front at $\zeta_d = R^2/t \approx 5.4 \times 10^{-7}$ m^2/s (Fig. 3). In the region $\zeta < \zeta_d$, all liquid phase has been removed by dissolution into the flowing CO_2 stream, while the intermediate region $\zeta_d \le R^2/t \le \zeta_f$ is the two-phase zone. In spite of space and time discretization errors, the simulation produces remarkably sharp fronts. This is due to the self-sharpening nature of the fronts (Pruess and Spycher, 2007), which counteracts numerical dispersion effects. In the simulation, salt precipitation occurs only in the innermost grid block in which an aqueous phase is present. It is in this block where most water uptake into the flowing CO_2 stream takes place, so that the gas phase reaches the next downstream block in essentially water-saturated conditions. Actually, there is a slight additional water uptake by the gas phase beyond the first (innermost) grid block with aqueous phase. This occurs because the next block downstream has smaller salinity, and correspondingly slightly larger equilibrium water concentration in the CO_2-rich phase; however, this effect is small and is not sufficient to initiate precipitation in the downstream block (Pruess and Spycher, 2007).

<Fig. 3 here>

<Fig. 4 here>

<Fig. 5 here>

For comparison we also performed a simulation in which no allowance was made for permeability reduction effects from salt precipitation. This produced saturation distributions that were practically indistinguishable from Figs. 3-4, but gave much lower pressures at small R^2/t (small radial distances or late time; see Fig. 5), highlighting the extent to which fluid pressurization could be reduced if precipitation could be avoided. This issue will be taken up in the next section.

The numerical simulation results indicate that solid saturation in the dry-out region is constant throughout (Fig. 4). This remarkable feature can be proven directly from the similarity property, as follows. Assume that dry-out at distance R occurs at some time t_1, at which time solid saturation is $S_S(R, t_1) = S_S(\zeta_1=R^2/t_1) = S_{S,1}$. Subsequent to dry-out, there can be no further change of solid saturation at R. Then $S_{S,1}$ must persist for all times $t > t_1$, so that $S_S(\zeta) = S_{S,1}$ holds for all $\zeta = R^2/t < \zeta_1$. This argument can be made for any dry-out distance R, showing that in the dry-out region, S_S will be independent of ζ.

The simulated value of solid saturation is $S_S = 9.1$ %, while in-place precipitation of all dissolved NaCl would yield a solid saturation of

$$S_{S,a} = \frac{\rho_{aq} X_s}{\rho_s} \tag{6}$$

where ρ_{aq} is aqueous phase density, X_s is mass fraction of dissolved salt in the aqueous phase, and ρ_s is density of precipitated salt. Inserting applicable parameters of $\rho_{aq} \approx 1180$ kg/m^3, $X_S = 0.25$, and $\rho_S = 2153$ kg/m^3 (Battistelli et al., 1997) we find $S_{S,a} = 13.7$ %, indicating that approximately (9.1/13.7 =) 66.4 % of solutes are precipitating, while the remainder is maintained in solution as brine is displaced outward by the CO_2. The brine that is displaced from the region in which salt precipitation is taking place has an NaCl concentration corresponding to the solubility limit of 26.5 % by weight at a temperature of 50 ºC. Part 2 of this series will explain

the fraction of solute precipitating in terms of the two-phase displacement process that removes part of the aqueous phase from the dry-out region where precipitation is occurring.

3. Fresh-Water Pre-flush as a Means to Control Precipitation Effects

Most of the pressurization seen in the preceding simulation occurred in the immediate vicinity of the injection well, where permeability is severely reduced by salt precipitation. This leads to the suggestion of pre-flushing with fresh water prior to CO_2 injection, to try to remove precipitable solutes from the vicinity of the injection well. Of course, care needs to be taken that such pre-flush will not have other adverse effects. For example, in formations with abundant clay minerals, fresh-water pre-flush may not be a good idea, because it may induce clay swelling resulting in permeability loss that may be worse than precipitation effects. Also, water injection rates must be limited so as not to reach fracturing pressures.

We will now propose and evaluate a specific schedule for pre-flushing, to try to alleviate the permeability loss and excessive pressurization seen in the problem discussed in Sec. 2. Examining the wellbore pressure increase as a function of time shows that most of the pressure increase occurs in the first 100 days of injection (Fig. 6a). The precipitation front is at $R^2/t \approx 5.4 \times 10^{-7}$ m^2/s, which after 100 days corresponds to a radius of R = 2.17 m, with an enclosed pore volume of 177.5 m^3. We expect that we could avoid precipitation for about 100 days, if we would just flush the brine from this volume. In fact, flushing this volume with fresh water should delay onset of precipitation for somewhat longer than 100 days, because the fresh water will be partly displaced outward by the injected CO_2, mixing with and diluting resident brine. Based on these considerations we perform a pre-flush in which we inject a total of 177.5×10^3 kg of fresh water, corresponding to the desired volume of approximately 177.5 m^3. Injecting at the same rate of 5 kg/s as for CO_2, injection of this amount of water is accomplished in a mere 35,500 s, or 9.9 hours. Downhole pressure increases due to fresh water injection from an initial value of 120 bar to 134.8 bar. When fresh water injection is terminated after 9.9 hours, CO_2 injection commences immediately.

Results for bottomhole injection pressures versus time are shown in Fig. 6 on linear and logarithmic time scales, respectively, and are compared with the previous simulation without a

pre-flush, as well as with a simulation in which permeability reduction from precipitation is ignored. The different time scales serve to highlight different features. The linear time plot (Fig. 6a) shows that pressurization for the injection with pre-flush begins to exceed the no-permeability-reduction case only after more than 200 days, indicating a substantial delay of precipitation effects. Subsequent pressure rise is a small fraction of what was seen without pre-flush. The logarithmic plot (Fig. 6b) shows that at very early times, the simulation with pre-flush predicts considerably lower pressures than the simulation in which permeability reduction is ignored. Two effects contribute to this outcome; the fresh water around the well (1) has lower viscosity, facilitating its displacement by injected CO_2, and (2) has larger solubility for CO_2 than brine, thereby reducing the mass and volume of free-phase CO_2. The pressure "kink" in the pre-flush case at about 0.07 days (Fig. 6b) occurs as the leading front of the injected CO_2 advances beyond the near-well region with fresh water, and reaches the region where aqueous phase salinity and viscosity is larger, so that fluid mobility is reduced.

We can conclude that, in saline formations with low clay content, fresh water pre-flush is a viable technique for avoiding or reducing formation damage from salt precipitation. Much of the pressurization from permeability loss due to precipitation occurs in the immediate vicinity of the wellbore. It is remarkable that pre-flushing with a modest amount of fresh water over a brief time period of a few hours can greatly reduce and delay injection pressure buildup for years.

<Fig. 6 here>

4. Sensitivity Studies on Precipitation

We start by considering formation parameters as used for problem #3 of a recent code intercomparison study (Pruess et al., 2004). The specifications given in Fig. 1 still apply, except that we use a larger absolute permeability of 100 mD (10^{-13} m^2), in order to reduce pressure buildup from injection and facilitate exploring a broader range of injection rates and precipitation-sensitive parameters. Relative permeability parameters are $S_{lr} = 0.30$, $m = 0.457$, $S_{gr} = 0.05$. Problem variations that were explored include different injection rates and absolute permeabilities, including or ignoring capillary pressures and aqueous diffusion, and varying salinity of the brine.

Test calculations showed that saturation profiles for gas and solid precipitate are insensitive to permeability reduction effects, as long as these effects do not give rise to extreme pressurization, that in turn would alter fluid properties. Accordingly, in order to simplify modeling of precipitation effects, the simulations reported in this section were done without allowance for permeability reduction. In the Buckley-Leverett (1942) approximation of neglecting fluid compressibility, saturation profiles are independent of flow rate and formation permeability; consequently, under these conditions the only aspect of the displacement process affected by changes in rates and permeabilities is the fluid pressures. The first three simulations (Case 1, 2, and 3) listed in Table 2 demonstrate that, when ignoring capillary pressures, solid saturations arising from precipitation are practically independent of flow rate. These calculations as well as additional simulations not shown here demonstrated that saturation profiles indeed depend only on relative permeability and viscosity parameters when capillary effects are neglected, indicating that deviations from the Buckley-Leverett fractional flow theory are small, even though supercritical CO_2 has significant compressibility.

Inclusion of capillary pressures (parameters P_0 = 19.61 kPa, S_{lr} = 0.0, S_{ls} = 0.999, λ = 0.457; see Eq. 2) causes an increase in precipitation, with increases in solid saturation ranging from ΔS_S = 0.25 % for the highest rate to 0.73 % for the lowest (Table 2, Cases 4-6). This can be understood from the fact that capillary pressures will provide a driving force for drawing water towards regions with higher gas saturations, adding a flow component that opposes the generally outward flow, especially near the dry-out front where capillary pressure gradients are largest. The aqueous phase flowing under capillary force in the direction of the injection well carries additional solutes with it that eventually will precipitate when dry-out is reached. Phase saturations and associated capillary pressure profiles are essentially independent of flow rate, which explains why capillary flow effects will have larger relative impacts when injection rates are lower. Increasing porosity (Case 7) slows temporal changes, but appears to leave S_S unchanged (compare Case 1); an explanation for this will be provided in Part 2. Of course, for larger porosity there is more precipitation, as the volume of solid precipitate per unit reservoir volume, ϕS_S, is directly proportional to porosity. Aqueous diffusion (Case 8), using an effective diffusion coefficient (Eq. A.6) of $\tau_0 \tau_\beta d_\beta^\kappa = 10^{-9}$ m^2/s for dissolved NaCl, has negligible effects

on solids precipitation (compare with Case 4). Reducing injection rate and formation permeability simultaneously by the same factor (Case 9 compared with Case 4) will leave pressure profiles unchanged, but it does alter the competition between outward flow of aqueous phase forced by the displacement process, and opposing flow driven by capillarity. Accordingly, there is slightly more precipitation in Case 9 than in Case 1.

Case 10 examines effects of reduced salinity. Comparison with Case 2 shows that reducing salinity by a factor 2 reduces solid saturation overproportionately by a factor of 2.23. An explanation for this response will be given in Part 2 on the basis of an analytical model for solids precipitation.

Case 11 has the same parameters as Case 1, except that irreducible liquid saturation S_{lr} in the relative permeability function Eq. (1) was increased from 0.3 to 0.4. This will reduce the amount of liquid that can be moved by immiscible displacement, and increase the proportion of liquid that is removed by dissolution into the CO_2 stream. As expected, this results in an increase in precipitation.

<Table 2 here>

5. 2-D Flow with Gravity Effects

Gravity effects on solids precipitation are explored by modeling CO_2 injection into a 2-D R-Z system. To limit the number of grid blocks we use coarser gridding than in the 1-D system (see Table 3), and we also specify a smaller thickness of 10 m for the aquifer, which we discretize into 10 layers of 1 m thickness each. In these simulations we include the wellbore in the grid, for a total of 101 grid blocks per layer. The total injection rate is distributed among the different reservoir layers in a manner that accounts for vertical pressure profiles as well as for fluid mobility (see Appendix B).

<Table 3 here>

We ran 2-D simulations for homogeneous porous media using similar parameters and variations as for the 1-D case. Results for two cases including capillary pressure with parameters as in Case 4 (Sec. 4) and injection rates of 2.5 and 0.25 kg/s, respectively, are given in Figs. 7-8. (We reduced injection rates in comparison with the 1-D model, because the 2-D model has only 1/10 the thickness.) Effects of gravity override on gas saturation distributions are strong, especially on a larger spatial scale (Fig. 7). Gravity override becomes more prominent when injection rates are reduced, because this reduces horizontal components of injection-induced pressurization, while buoyancy forces remain unaffected. For the larger injection rate, the outflow profile from the injection well is nearly uniform (Fig. 8), so that flow is approximately 1-D near the well, and gravity override is almost exclusively due to buoyant flow in the formation. In contrast, at the lower rate outflow is considerably stronger near the top of the injection well (Fig. 8), so that both buoyancy effects in the formation and outflow profiles from the wellbore contribute to CO_2 preferentially accumulating near the top of the permeable interval. We note that outflow profile effects will be considerably stronger in aquifers with greater thickness than the H = 10 m that was assumed in our 2-D simulations.

<Fig. 7 here>

<Fig. 8 here>

For the larger-rate case, precipitation is fairly uniform (lower panel in Fig. 7a). Average solid saturation is approximately 7.1 %, with slightly lower solid saturations near the top, and a small region of slightly higher S_S near the bottom. The value of S_S = 7.1 % is almost identical to the result for the 1-D Case 4. Somewhat larger S_S right near the wellbore are due to space discretization effects. Rather different precipitation behavior is seen at the lower rate (lower panel in Fig. 7b). Average solid saturations are somewhat larger now, due to the stronger role of capillary pressures at lower rates (compare the trends from Case 4-6, Table 2). The main differences to the higher-rate case, however, are in the pronounced vertical solid saturation trend, and the emergence of a localized region with very large solids precipitation near the lower portion of the dry-out front. The latter behavior had been noted previously by Giorgis et al. (2007); it is caused by persistent capillary-driven backflow of aqueous phase towards the

injection well in this region, which provides a continuous supply of precipitable solids. The accumulation of solids in this region exacerbates gravity override effects, as it suppresses CO_2 outflow near the bottom of the aquifer, instead funneling CO_2 upwards.

To better appreciate the role of capillary-driven backflow in shaping the pattern of solids precipitation, another simulation was performed for the low-rate (0.25 kg/s) case in which capillary pressure was neglected. This produced a largely featureless distribution (not shown) in which solid saturation throughout the entire region in which precipitation occurred was nearly uniform at $S_S = 6.5\ \% \pm 0.5\ \%$. Only in a small region (fraction of a meter) near the bottom of the permeable interval did S_S reach a maximum of 12.4 %; in contrast, the simulation with capillary pressure generated S_S in excess of 20 % in a region with linear dimension of several meters (lowest panel in Fig. 7b). In spite of these large differences in precipitation patterns, the total amount of precipitated solids was almost identical in both cases, being just 1.0 % larger when capillary pressures were included.

6. Concluding Remarks

Injection of CO_2 into saline aquifers will induce complex coupled processes on multiple scales. In highly saline environments, formation dry-out around the injection well is a concern, because it may induce precipitation of salts with attendant loss of porosity, permeability, and injectivity. The progression of dry-out and precipitation may depend on many factors, including CO_2 injection rate; aquifer properties such as porosity, absolute and relative permeability, and capillary pressure; and on thermodynamic conditions in the injection interval (aquifer temperature, pressure, and fluid composition). Formation heterogeneities may play a strong role in how dry-out and precipitation play out, by directing, containing, and channeling the injected CO2.

This first paper ("Part 1") in a two-part series explored fundamental aspects of formation dry-out and salt precipitation, using detailed simulations of the relevant multiphase flow and interphase mass transfer processes. These processes are multi-scale in space and time, and understanding of precipitation dynamics is greatly aided by a similarity property that holds under well-defined restrictions. Specifically, the governing equations for non-isothermal multiphase

flow may be rigorously transformed into ordinary differential equations in the "similarity variable" $\zeta = R^2/t$ (O'Sullivan, 1981), when the following conditions are satisfied, (1) 1-D radial flow with constant-rate injection, (2) homogeneous porous medium with uniform initial conditions, and (3) thermodynamic equilibrium locally (i.e., no precipitation kinetics; instantaneous composition equilibrium between aqueous and CO_2-rich phases). The similarity property holds even when taking all of the non-linear processes and fluid property variations into account, such as non-linear relative permeabilities and capillary pressures, and mass transfer between fluid phases. The similarity property dictates that the space-and-time evolution of the system depends on distance R and time t only through the similarity variable $\zeta = R^2/t$. This is extremely useful as it allows to connect spatial and temporal changes in a manner that is fully scalable (large t corresponding to small R and vice versa).

Our simulations show that precipitation occurs only in the dry-out region around the injection well, but not in the two-phase zone beyond the dry-out region. This observation is explained from the thermodynamics of interphase mass transfer, which constrains salinity increase beyond the dry-out front, as in the two-phase zone little additional water can dissolve into the CO_2-rich phase. From the general (self-sharpening) nature of the dry-out front and the similarity property we can deduce that "solid saturation S_S" - the fraction of pore space filled by solid precipitate - is constant behind the dry-out front. Part 2 (this volume) will present a simple mathematical model that allows to directly calculate solid saturation S_S from fluid properties and multiphase flow properties of the formation, without having to carry out a flow simulation.

For 1-D radial flow under the similarity property constraints mentioned above, our simulations have established the following,

- precipitation occurs only behind a sharp dry-out front;
- solid saturation S_S (fraction of pore space filled by precipitate) throughout the dry-out region is constant, independent of space and time; (The value of this constant depends on problem parameters.)
- for a fixed quantity of CO_2 injected into a medium with given characteristics, saturation profiles are essentially independent of injection rate; (We note that independence of

saturations from rates would be expected under the assumption of incompressible flow (Buckley and Leverett, 1942); so even though CO_2 has significant compressibility, the incompressibility assumption is approximately valid.)

- inclusion of capillary pressure effects will increase solids precipitation by a factor of order 1.1 or less.

When CO_2 is injected into realistic heterogeneous media, the induced processes of multiphase flow, formation dry-out and salt precipitation will of course become more complex. For example, clay or silt lenses could provide longer-term sources of brine that would be driven by capillary suction to drying regions of coarser and more permeable material. The present study of precipitation in homogeneous media may provide building blocks for scale-up to fully 3-D flows in heterogeneous reservoir domains.

The possibility of using a brief pre-flush with fresh water to displace precipitable solids away from the injection well was considered, as a means to delay onset of precipitation and reduce its severity, thereby reducing permeability and injectivity loss, and fluid pressurization. Our simulations suggest that the strongest impacts of precipitation on injectivity are typically confined to a region of just a few meters around the injection well, and it is found that a brief pre-flush of just a few hours is able to achieve surprisingly large and long-term benefits.

Two-dimensional simulations of CO_2 injection show gravity override that becomes increasingly strong when injection rates are reduced. Gravity and capillary effects tend to slow the advancement of the CO_2 displacement front near the bottom of the injection interval. Limited outflow of CO_2 in this region accompanied by capillary-driven backflow of water may produce an almost stationary dry-out front, with large localized precipitation that amplifies effects of gravity override.

Appendix A. Governing Equations

The basic mass conservation equations governing the flow of multiphase, multicomponent fluids in permeable media can be written in the following form.

$$\frac{d}{dt}\int_{V_n} M^\kappa \, dV_n \quad = \quad \int_{\Gamma_n} \mathbf{F}^\kappa \bullet \mathbf{n} \, d\Gamma_n + \int_{V_n} q^\kappa dV_n \tag{A.1}$$

The integration is over an arbitrary subdomain V_n of the flow system under study, which is bounded by the closed surface Γ_n. The quantity M appearing in the accumulation term (left hand side) represents mass per volume, with $\kappa = 1, ..., NK$ labeling the components (water, NaCl, CO_2). **F** denotes mass flux (see below), and q denotes sinks and sources. **n** is a unit normal vector on surface element $d\Gamma_n$, pointing inward into V_n. Eq. (A.1) expresses the fact that the rate of change of fluid mass in V_n is equal to the net inflow across the surface of V_n, plus net gain from fluid sources.

The general form of the accumulation term is

$$M^\kappa \quad = \quad \phi \sum_\beta S_\beta \rho_\beta X_\beta^\kappa \tag{A.2}$$

In Eq. (A.2), the total mass of component κ is obtained by summing over the fluid and solid phases β (= liquid, gas, solid). ϕ is porosity, S_β is the saturation of phase β (i.e., the fraction of pore volume occupied by phase β), ρ_β is the density of phase β, and X_β^κ is the mass fraction of component κ present in phase β.

Advective mass flux is a sum over phases,

$$\mathbf{F}^\kappa\Big|_{adv} \quad = \quad \sum_\beta X_\beta^\kappa \mathbf{F}_\beta \tag{A.3}$$

and individual phase fluxes are given by a multiphase version of Darcy's law:

$$\mathbf{F}_\beta = \rho_\beta \mathbf{u}_\beta = -k \frac{k_{r\beta} \rho_\beta}{\mu_\beta} (\nabla P_\beta - \rho_\beta \mathbf{g}) \quad (A.4)$$

Here $\mathbf{u}_\beta$ is the Darcy velocity (volume flux) in phase β, k is absolute permeability, $k_{r\beta}$ is relative permeability to phase β, μ_β is viscosity, and

$$P_\beta = P + P_{c\beta} \quad (A.5)$$

is the fluid pressure in phase β, which is the sum of the pressure P of a reference phase (usually taken to be the gas phase), and the capillary pressure $P_{c\beta}$ (≤ 0). $\mathbf{g}$ is the vector of gravitational acceleration. Our TOUGH2 simulator also considers diffusive fluxes in all phases, and includes coupling between diffusion and phase partitioning that can be very important for volatile solutes in multiphase conditions (Pruess, 2002). Diffusive flux of component κ in phase β is given by

$$\mathbf{f}_\beta^\kappa = -\phi \tau_0 \tau_\beta \rho_\beta d_\beta^\kappa \nabla X_\beta^\kappa \quad (A.6)$$

where $\tau_0\tau_\beta$ is the tortuosity which includes a porous medium dependent factor τ_0 and a coefficient that depends on phase saturation S_β, $\tau_\beta = \tau_\beta(S_\beta)$, and d_β^κ is the diffusion coefficient of component κ in bulk fluid phase β. Special TOUGH2 versions that include a conventional Fickian model for hydrodynamic dispersion have also been developed, but dispersion is not modeled in the present study.

Multiphase flows often involve strong heat transfer effects, requiring consideration of an energy balance along with mass balances. Equations similar to the foregoing can be formulated for energy conservation and are given in the TOUGH2 user's guide (Pruess et al., 1999).

By applying Gauss' divergence theorem, Eq. (A.1) can be converted into the following partial differential equation (PDE)

$$\frac{\partial M^{\kappa}}{\partial t} = -\mathrm{div}\mathbf{F}^{\kappa} + q^{\kappa} \qquad \text{(A.7)}$$

which is the form commonly used as the starting point for deriving finite difference or finite element discretization approaches. However, in TOUGH2 we use an "integral finite difference" method (Narasimhan and Witherspoon, 1976), in which space discretization is directly applied to the integrals in Eq. (1).

The calculation of thermophysical properties for water/NaCl/ CO_2 mixtures appearing in the equations given above is described in the ECO2N user's guide (Pruess, 2005).

Appendix B. Wellbore Flow Connections in the Integral Finite Difference Method

When a wellbore intersects several grid layers, the issue arises how to allocate total injection rate to the individual layers. A possible prescription is to allocate injection rates according to the kH (permeability-thickness) product. For a total injection rate q, the portion that would be injected into layer i would be

$$q_i = \frac{k_i H_i}{\sum_j k_j H_j} q \qquad \text{(B.1)}$$

However, because of the often substantially smaller density of the CO_2 in the wellbore as compared to formation fluids (brine), the vertical pressure gradient in the wellbore will be smaller than in the formation, and the horizontal component of the gradient that drives fluids from the wellbore will become smaller for deeper layers. Accordingly, we expect the shallower layers to take more fluid than based on fractional kH, and we do not expect Eq. (B.1) to provide a good approximation for CO_2 injection into brine aquifers.

An alternative approach would be to include the wellbore itself into the computational grid as a region of very high permeability, and discretize it into the same layering as used for the formation. This is shown in Fig. B.1a, which also indicates that the nodal points for the wellbore should be placed near the interface with the first column of formation grid blocks, to reduce the length of the flow path within the wellbore to infinitesimal size and thereby avoid unphysical flow resistance. The approach portrayed in Fig. B.1a has the drawback that it requires explicit treatment of flows between small wellbore grid blocks of very high permeability, which can severely limit time steps during the simulation. In the 2-D simulations presented in this paper we use an alternative approach illustrated in Fig. B.1b, which represents the entire wellbore as a single grid block, and directly evaluates flows between that single block and the several grid blocks in the column adjacent to the well. In the integral finite difference (finite volume) method used here (Narasimhan and Witherspoon, 1976), the effective pressure gradient between grid blocks labeled 1 and 2 is written as follows (see Fig. B.2).

$$\left(\nabla P\right)_{eff} \quad = \quad \frac{P_2 - P_1}{D_1 + D_2} + \rho_{12} g \cos\gamma \tag{B.2}$$

where ρ_{12} is the average of densities (evaluated separately for each fluid phase) between grid blocks 1 and 2, and γ is the angle between the nodal line connecting blocks 1 and 2 and the vertical (positive if block 2 is at higher elevation than point 1, see Fig. B.2). Equation (B.2) gives the component of effective gradient in the direction of the nodal line, and its application requires that the interface between 1 and 2 be perpendicular to the nodal line. We now generalize Eq. (B.2) by writing $\cos\gamma = \left(Z_2 - Z_1\right)/\left(D_1 + D_2\right)$, where $Z_{1,2}$ are the respective grid block elevations, and apply this even under conditions where the line connecting nodal points 1 and 2 is not perpendicular to their common interface (see the dashed nodal line in Fig. B.1b). The effective pressure gradient for flow between grid blocks 1 and 2 is then written

$$\left(\nabla P\right)_{eff} \quad = \quad \frac{P_2 - P_1}{D_1 + D_2} + \rho_{12} g \frac{Z_2 - Z_1}{D_1 + D_2} \tag{B.3}$$

D_1 and D_2 are interpreted as distances of the nodal points from the interface, so that the expression $\left(Z_2 - Z_1\right)/\left(D_1 + D_2\right)$ in general may now be larger than 1, as is the case e.g. for points 1 and 2 in Fig. B.1b. For "normal" flow connections that conform to the constraint that the interface be perpendicular to the nodal line, Eq. (B.3) is identical to (B.2). To appreciate the physical significance of Eq. (B.3) for non-conforming connections, such as marked by the dashed line in Fig. B.1b, multiply Eq. (B.3) by the sum of nodal distance, D_1+D_2, to obtain

$$\left(P_2 - P_1\right)_{eff} \quad = \quad P_2 - \left(P_1 - \rho_{12} g\left[Z_2 - Z_1\right]\right) \tag{B.4}$$

This shows that Eq. (B.3) performs a straight gravity correction of pressures in the wellbore, effectively defining flow between grid blocks 1 and 2 based on the pressure gradient between nodal point 2 and the interpolation node opposite to point 2, that is marked with an x at an elevation [Z_2 - Z_1] above point 1 in Fig. B.1b. Equation (B.3) is easily implemented into our TOUGH2 simulator, allowing distribution of flow out of a wellbore to multiple layers with proper consideration of elevation differences and associated gravity effects. Differences in

absolute permeabilities and fluid mobilities in different layers are of course automatically considered in TOUGH2 when adopting an effective pressure gradient as given by Eq. (B.3).

<Fig. B.1 here>

<Fig. B.2 here>

Acknowledgement

Thanks are due to Christine Doughty for a careful review of the manuscript and the suggestion of improvements. We also thank two anonymous reviewers for their comments and suggestions. This work was supported by the Zero Emission Research and Technology project (ZERT) under Contract No. DE-AC02-05CH11231 with the U.S. Department of Energy.

References

André, L., P. Audigane, M. Azaroual and A. Menjoz. Numerical Modeling of Fluid–rock Chemical Interactions at the Supercritical CO2–liquid Interface during CO2 Injection into a Carbonate Reservoir, the Dogger Aquifer (Paris Basin, France), *Energy Conv. Mgmt.,* Vol. 48, No. 6, pp. 1782–1797, 2007.

Battistelli, A., C. Calore and K. Pruess. The Simulator TOUGH2/EWASG for Modeling Geothermal Reservoirs with Brines and Non-Condensible Gas, *Geothermics*, Vol. 26, No. 4, pp. 437 - 464, 1997.

Buckley, S.E. and M.C. Leverett. Mechanism of Fluid Displacement in Sands, *Trans. Am. Inst. Min. Metall. Eng.,* Vol. 146, pp. 107 - 116, 1942.

Carsel, R.F. and R.S. Parrish. Developing Joint Probability Distributions of Soil Water Retention Characteristics, *Water Resour. Res.,* Vol. 24, No. 8, pp. 755 - 769, 1988.

Corey, A.T. The Interrelation Between Gas and Oil Relative Permeabilities, *Producers Monthly*, pp. 38 - 41, November 1954.

Doughty, C. and K. Pruess. A Similarity Solution for Two-Phase Water, Air and Heat Flow Near a Linear Heat Source in a Porous Medium, *J. of Geophys. Res.*, Vol. 97 (B2), pp. 1821 - 1838, 1992.

Fuller, R.C., J.H. Prevost and M. Piri. Three-Phase Equilibrium and Partitioning Calculations for CO2 Sequestration in Saline Aquifers, *J. Geophys. Res.,* Vol., 111, B06207, doi:10.1029/2005JB003618, 2006.

Giorgis, T., M. Carpita and A. Battistelli. 2D Modeling of Salt Precipitation During the Injection of Dry CO2 in a Depleted Gas Reservoir, *Energy Conv. Managemt.,* Vol. 48, pp. 1816–1826, 2007.

Hurter, S., D. Labregere and J. Berge. Simulations for CO2 Injection Projects with Compositional Simulator, paper SPE-108540, presented at Offshore Europe 2007 conference of the Society of Petroleum Engineers, Aberdeen, Scotland, September 2007.

Kleinitz, W., M. Koehler and G. Dietsch. The Precipitation of Salt in Gas Producing Wells, paper SPE-68953, presented at the SPE European Formation Damage Conference, The Hague, The Netherlands, May 2001.

Lorenz, S. and W. Müller. Modelling of Halite Formation in Natural Gas Storage Aquifers, *Proceedings, TOUGH Symposium 2003,* Lawrence Berkeley National Laboratory, Berkeley, CA, May 2003.

Narasimhan, T.N. and P.A. Witherspoon. An Integrated Finite Difference Method for Analyzing Fluid Flow in Porous Media, *Water Resour. Res.*, Vol. 12, No. 1, pp. 57–64, 1976.

O'Sullivan, M.J. A Similarity Method for Geothermal Well Test Analysis, *Water Resour. Res.*, Vol. 17, No. 2, pp. 390 – 398, 1981.

Pape, H., C. Clauser and J. Iffland. Permeability Prediction Based on Fractal Pore-Space Geometry, *Geophysics,* Vol. 64, No. 5, pp. 1447 - 1460, 1999.

Press, W.H., B.P. Flannery, S.A. Teukolsky, and W.T. Vetterling. *Numerical Recipes, The Art of Scientific Computing*, Cambridge University Press, Cambridge, London, New York, 1986.

Pruess, K. Numerical Simulation of Multiphase Tracer Transport in Fractured Geothermal Reservoirs, *Geothermics,* Vol. 31, pp. 475 - 499, 2002.

Pruess, K. The TOUGH Codes—A Family of Simulation Tools for Multiphase Flow and Transport Processes in Permeable Media, *Vadose Zone J.,* Vol. 3, pp. 738 - 746, 2004.

Pruess, K. ECO2N: A TOUGH2 Fluid Property Module for Mixtures of Water, NaCl, and CO2, Lawrence Berkeley National Laboratory Report LBNL-57952, Berkeley, CA, June 2005. (http://www-esd.lbl.gov/TOUGH2/eco2n_man.pdf)

Pruess, K., C. Oldenburg and G. Moridis. TOUGH2 User's Guide, Version 2.0, Lawrence Berkeley National Laboratory Report LBNL-43134, Berkeley, CA, November 1999.

Pruess, K. and J. García. Multiphase Flow Dynamics During CO2 Injection into Saline Aquifers, *Environmental Geology,* Vol. 42, pp. 282 - 295, 2002.

Pruess, K., J. García, T. Kovscek, C. Oldenburg, J. Rutqvist, C. Steefel and T. Xu. Code Intercomparison Builds Confidence in Numerical Simulation Models for Geologic Disposal of CO2, *Energy,* Vol. 29, Issues 9-10, pp. 1431-1444, doi:10.1016/j.energy.2004.03.077, July-August 2004.

Pruess K. and N. Spycher. ECO2N – A Fluid Property Module for the TOUGH2 Code for Studies of CO2 Storage in Saline Aquifers, *Energy Conversion and Management,* Vol. 48, No. 6, pp. 1761–1767, doi:10.1016/j.enconman.2007.01.016, 2007.

Spycher, N. and K. Pruess. CO_2-H_2O Mixtures in the Geological Sequestration of CO_2. II. Partitioning in Chloride Brines at 12–100 °C and up to 600 bar, *Geochim. Cosmochim. Acta,* Vol. 69, No. 13, pp. 3309–3320, doi:10.1016/j.gca.2005.01.015, 2005.

van Genuchten, M.Th. A Closed-Form Equation for Predicting the Hydraulic Conductivity of Unsaturated Soils, *Soil Sci. Soc. Am. J.*, Vol. 44, pp. 892 - 898, 1980.

Vaughan, P.J., D.E. Moore, C.A. Morrow and J.D. Byerlee. Role of Cracks in Progressive Permeability Reduction During Flow of Heated Aqueous Fluid Through Granite, *J. Geophys. Res.*, Vol. 91, No. B7, pp. 7517–7530, 1986.

Verma, A. and K. Pruess. Thermohydrologic Conditions and Silica Redistribution Near High-Level Nuclear Wastes Emplaced in Saturated Geological Formations, *Journal of Geophysical Res.*, Vol. 93 (B2), pp. 1159-1173, 1988.

Xu, T., Y. Ontoy, P. Molling, N. Spycher, M. Parini and K. Pruess. Reactive Transport Modeling of Injection Well Scaling and Acidizing at Tiwi Field, Philippines, *Geothermics,* Vol. 33, No. 4, pp. 477 - 491, 2004.

Xu, T., J. A. Apps, K. Pruess, and H. Yamamoto, Numerical modeling of injection and mineral trapping of CO2 with H2S and SO2 in a sandstone formation, *Chemical Geology,* 242/3-4, pp. 319-346, 2007.

Tables

Table 1. Space discretization for the 1-D radial grid.

cumulative radial distance (m)	space discretization
0.1	wellbore radius R_w
10	495 increments with $\Delta R = 0.02$ m
10^3	200 increments with $\Delta R_{n+1} = c_1 \times \Delta R_n$ ($c_1 = 1.0382608$)
10^4	100 increments with $\Delta R_{n+1} = c_2 \times \Delta R_n$ ($c_2 = 1.0159674$)
10^5	5 increments with $\Delta R_{n+1} = c_3 \times \Delta R_n$ ($c_3 = 3.2271821$)

Table 2. Sensitivitiy of solids precipitation to variations in process description and parameters.

Case	CO_2 rate (kg/s)	P_{cap}	Problem variation	S_S (%)
1	25	no		6.72
2	12.5	no		6.72
3	6.25	no		6.71
4	25	yes		6.97
5	12.5	yes		7.13
6	6.25	yes		7.47
7	25	no	increase porosity from 12 % ==> 30 %	6.72
8	25	yes	include diffusion in aq. phase	6.97
9	6.25	yes	k reduced to k/4	7.13
10	12.5	no	X_S reduced to $X_S/2$	2.97
11	25	no	irreducible liquid saturation S_{lr} increased from 0.3 to 0.4	7.57

Table 3. Space discretization for the 2-D radial grid.

cumulative radial distance (m)	space discretization
0	origin
0.1	wellbore radius R_w
10	70 increments with $\Delta R_{n+1} = c_1 \times \Delta R_n$, starting with $\Delta R = 0.02$ m $c_1 = 1.0464394$
10^2	10 increments with $\Delta R_{n+1} = c_2 \times \Delta R_n$ $c_2 = 1.5265184$
10^3	10 increments with $\Delta R_{n+1} = c_3 \times \Delta R_n$ $c_3 = 1.1850204$
10^5	10 increments with $\Delta R_{n+1} = c_4 \times \Delta R_n$ $c_4 = 1.7330721$

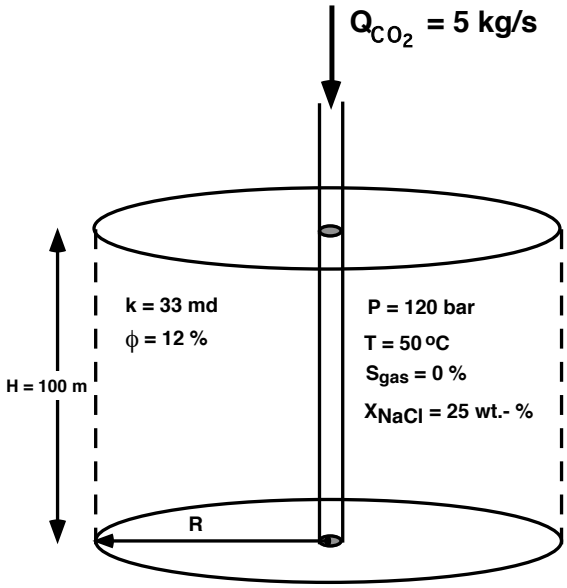

Figure 1. Schematic of 1-D radial injection problem (33 md = 33×10^{-15} m^2).

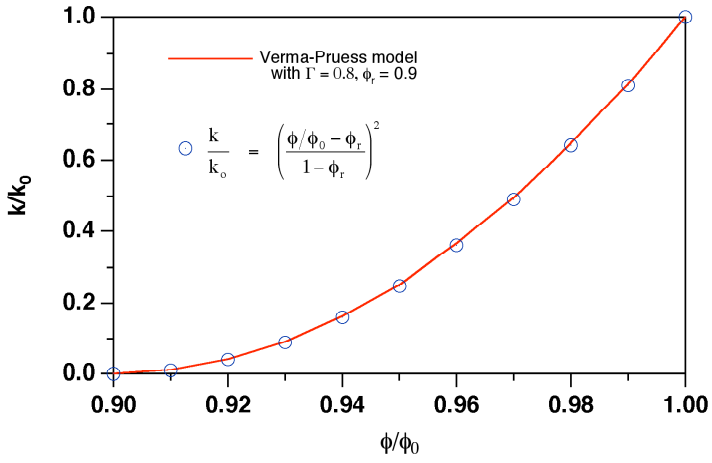

Figure 2. Relationship between porosity and permeability reduction, after Verma and Pruess (1988).

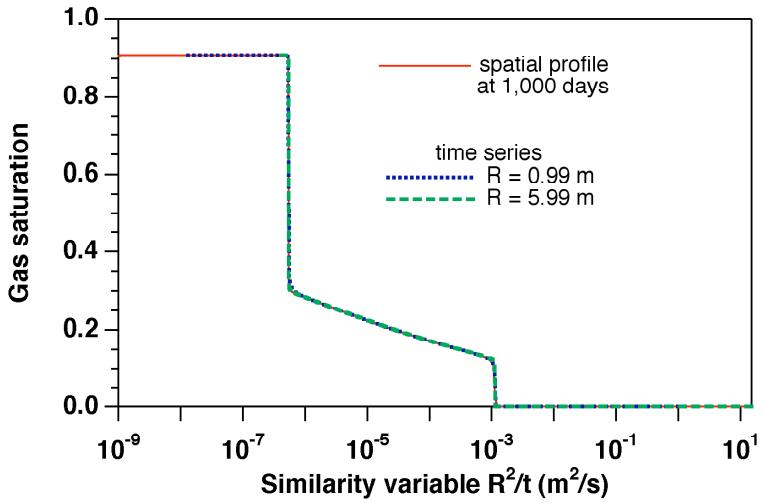

Figure 3. Gas saturation as function of the similarity variable.

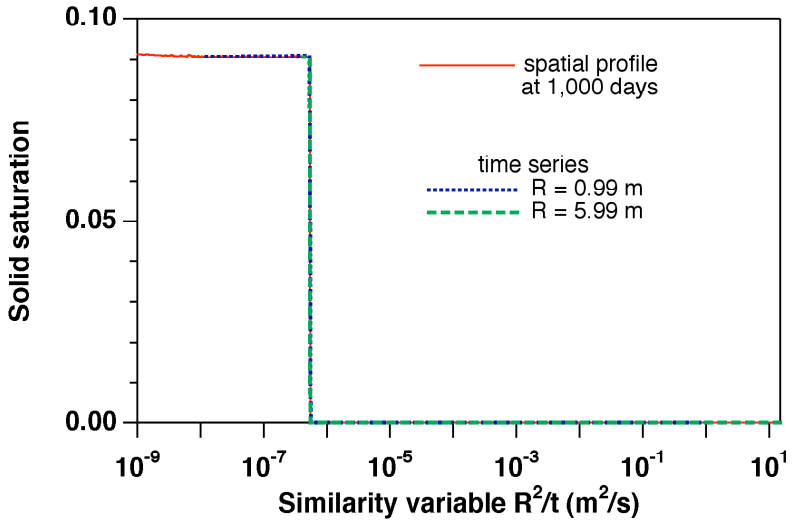

Figure 4. Solid saturation (fraction of pore volume containing solid precipitate) as function of the similarity variable.

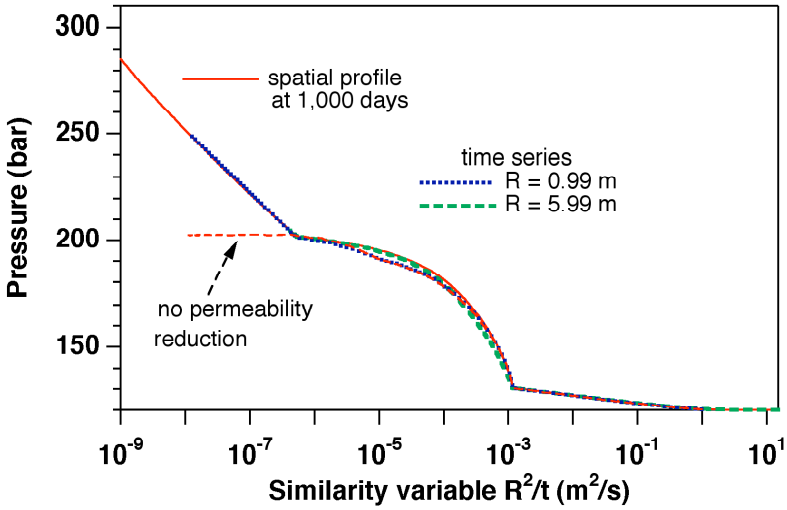

Figure 5. Fluid pressure as function of the similarity variable. A problem variation that neglects permeability reduction from precipitation is also shown.

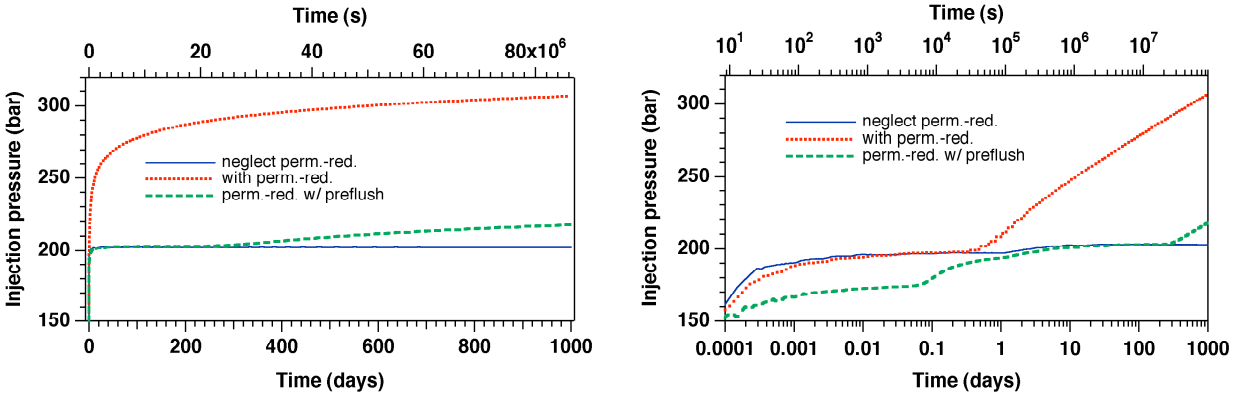

Figure 6. Simulated injection pressures for different assumptions about salt precipitation and permeability loss (a - linear time scale; b - logarithmic time scale).

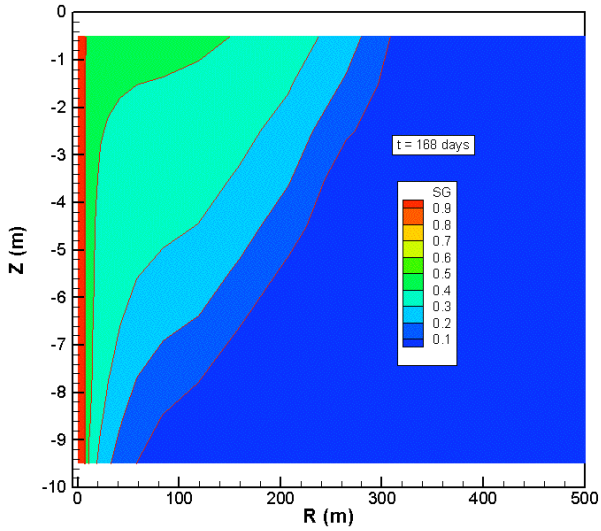
t = 168 days
SG
0.9
0.8
0.7
0.6
0.5
0.4
0.3
0.2
0.1
Z (m)
R (m)

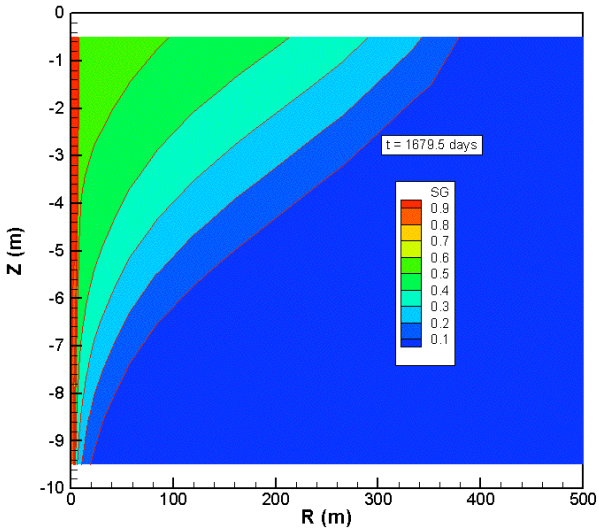
t = 1679.5 days
SG
0.9
0.8
0.7
0.6
0.5
0.4
0.3
0.2
0.1
Z (m)
R (m)

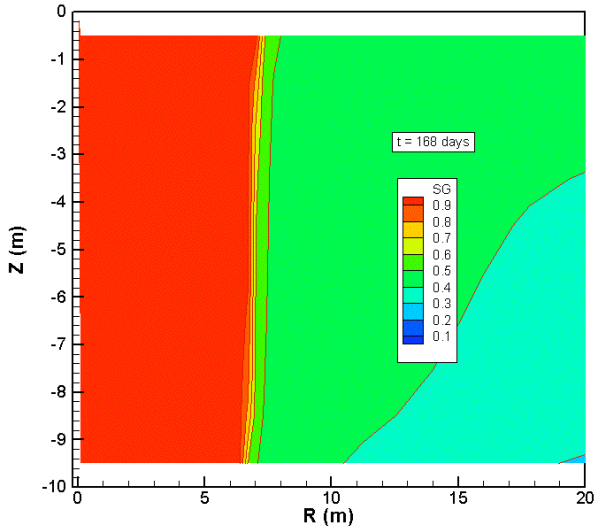
t = 168 days
SG
0.9
0.8
0.7
0.6
0.5
0.4
0.3
0.2
0.1
Z (m)
R (m)

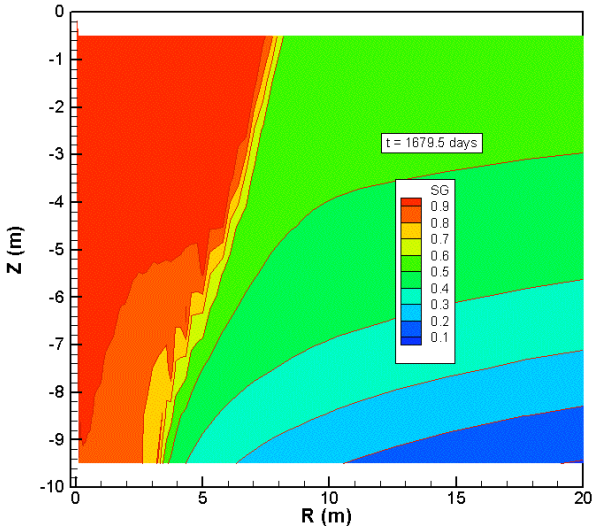
t = 1679.5 days
SG
0.9
0.8
0.7
0.6
0.5
0.4
0.3
0.2
0.1
Z (m)
R (m)

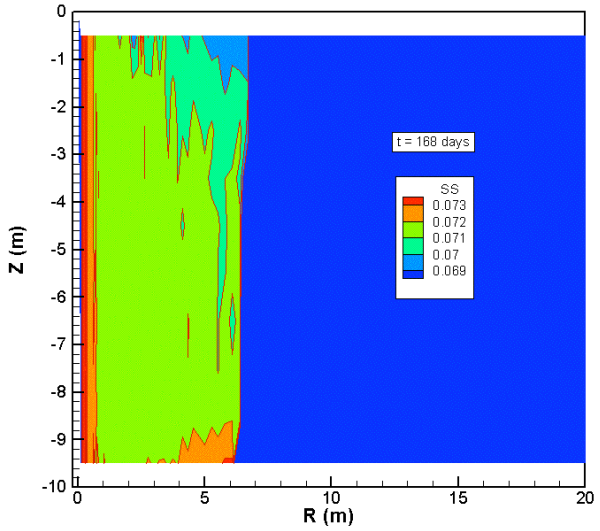
t = 168 days
SS
0.073
0.072
0.071
0.07
0.069
Z (m)
R (m)

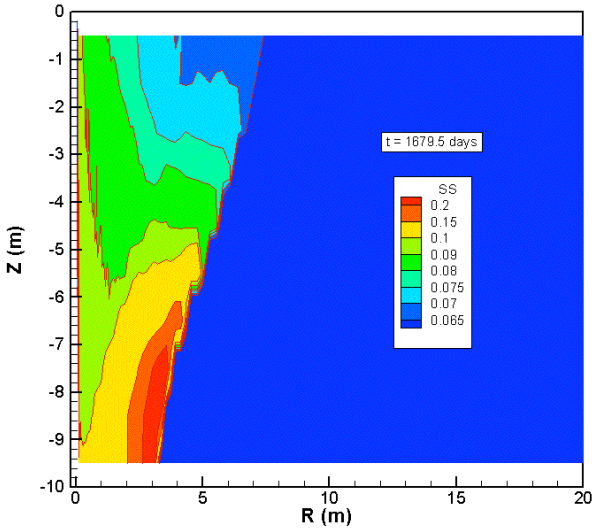
t = 1679.5 days
SS
0.2
0.15
0.1
0.09
0.08
0.075
0.07
0.065
Z (m)
R (m)

(a) (b)

Figure 7. Distribution of gas saturations (top four frames; note different radial scales) and solid saturations (bottom frames) for injection rates of 2.5 kg/s (a) and 0.25 kg/s (b). Total amount of CO_2 injected is the same in both cases.

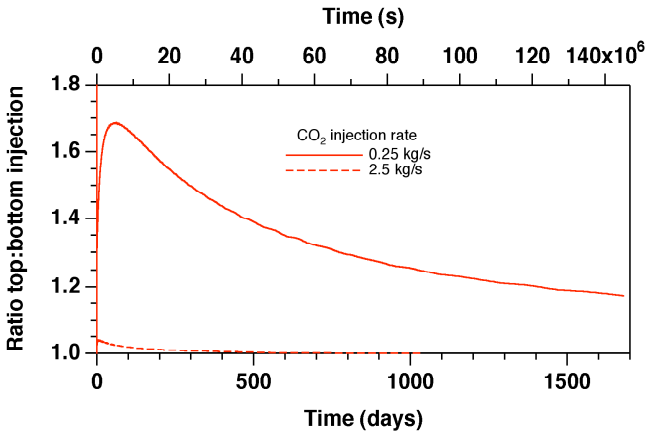

Figure 8. Ratio of injection rates into the top and bottom layers, for different total CO_2 injection rates.

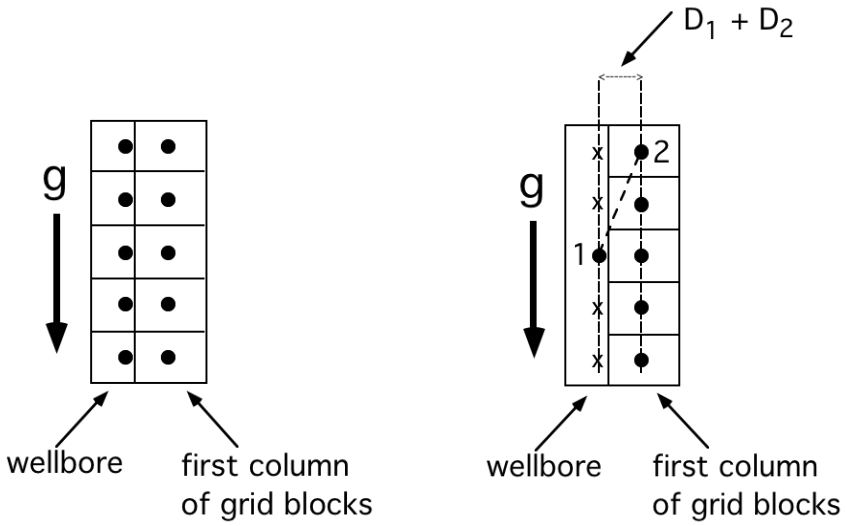

Figure B.1. Gridding near the wellbore in a 2-D R-Z flow system. (a) shows sub-gridding of the wellbore, while (b) models the wellbore as a single block, and introduces "interpolation nodes," marked by x. Nodal distances for blocks 1 and 2 are interpreted along lines drawn perpendicular to the interface. The direction of gravity acceleration **g** is also shown.

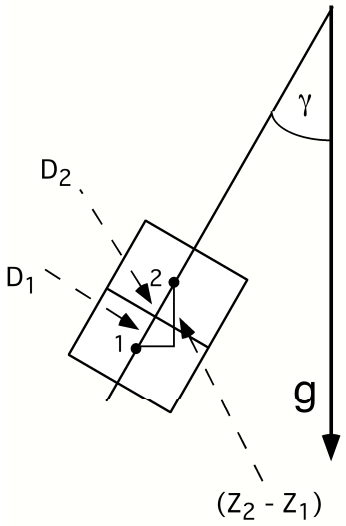

Figure B.2 Schematic of a non-horizontal flow connection between grid blocks 1 and 2 that conforms to the requirement that the nodal line be perpendicular to the interface. Some geometric parameters are shown.